



Effects of processing on microstructure evolution and fatigue crack growth mechanisms in cold-spray 6061 aluminum alloy

Anastasios G. Gavras^a, Diana A. Lados^a, Victor K. Champagne^b, Robert J. Warren^{a,*}

^a Worcester Polytechnic Institute, Integrative Materials Design Center, Worcester, MA 01609, USA

^b U.S. Army Research Laboratory, Aberdeen Proving Ground, MD 21005, USA



ARTICLE INFO

Keywords:

Cold-spray 6061 aluminum alloy
Microstructure
Heat treatment
Fatigue crack growth
Design maps

ABSTRACT

Owing to their fine microstructures, cold-spray processed alloys possess appealing static mechanical properties, similar to their wrought counterparts, making them potential candidates for structural applications. In spite of their great potential, the lack of knowledge of their cyclic behavior, especially the fatigue crack growth response, limits their use in high-integrity applications. Thus, further advanced characterization of cold-spray processed materials is needed. In this study, fatigue crack growth microstructural mechanisms were established for bulk cold-spray processed 6061 aluminum alloy tested in laboratory air at room temperature. The effects of the material's characteristic microstructure, stress ratio ($R = 0.1, 0.5$, and 0.7), and post-fabrication heat treatment (annealing and T6) on the fatigue crack growth behavior were systematically investigated. It was found that the initial powder particle characteristics play an important role in the crack's propagation through the cold-spray 6061 microstructures, and particle boundaries are critical in the materials' response, especially at high driving force. To aid the material-process design, two crack tip driving force parameter maps that relate loading conditions to damage at the microstructure scale were also established. Furthermore, a Paris-type, microstructure-based model was successfully developed to predict the fatigue crack growth rates in upper Region II and Region III for the as-fabricated and annealed materials. Discussions related to the use of these materials for fatigue-critical applications are also provided.

1. Introduction

Cold-spray processing, along with more established spray processes such as thermal spraying, are often used as coating techniques to improve the surface properties of metallic materials. However, the unique characteristics of cold-spray materials warrant the possible use of the process as an additive manufacturing (AM) technique for building 3D structural components. While the process is neither as precise as selective melting techniques, nor as fast as direct deposition methods, the solid state nature of cold-spray processing sets it apart from more conventional spraying and AM methods. Cold-spray technology is thus the logical choice for applications where the high temperatures associated with conventional thermal spray technology are undesirable.

The cold-spray process works by introducing a powder feedstock into a high-pressure, elevated temperature chamber, and accelerating it in a gas stream via a converging-diverging de Laval nozzle towards the substrate, as shown in Fig. 1. Upon impact with the substrate, the powder particles are plastically deformed, and once a critical impact velocity is reached, bonding occurs due to adiabatic shear instability

[1,2]. Parameters that influence the critical velocity (and hence particle bonding) are the process temperature, gas conditions, nozzle geometry, type of sprayed material, and powder characteristics (e.g. particle density, size, and distribution) [3,4]. Gas temperature is particularly important in terms of variations in the residual stress and interface adhesion of the applied coating [5].

The cold-spray process requires very high particle velocities (up to 1500 m/s) to achieve consolidation [6,7]. Gas temperatures can be adjusted to avoid undesirable transformations in the feedstock, deposit, and the substrate, yielding a deposit with low porosity, high interparticle bond strength, and improved adhesion to the substrate. Substrate-coating adhesion occurs via two main mechanisms: deformation of the substrate by the impacting particles causing material mixing and mechanical interlocking, and metallurgical bonding between the substrate and coating by diffusion [8,9]. This is in contrast to the adhesion mechanisms of thermal spray coatings, which rely primarily upon the surface finish, referred to as the anchor tooth profile of the substrate. In thermal spraying, the molten particles, or 'splats', which are propelled onto the substrate, penetrate and subsequently solidify, locking

* Corresponding author.

E-mail address: r.j.warren@swansea.ac.uk (R.J. Warren).

Nomenclature	
a	crack length
ΔK_{eff}	closure corrected effective stress intensity factor range
ΔK_o	initial stress intensity factor range at the start of the test
m	Paris Law constant
m'	Paris-type Law constant used for linear crack growth model in upper Region II and Region III
N	number of fatigue cycles
N_C	average particle packing coordination number
r_p	crack tip plastic zone radius
R	stress ratio
σ_B	bond strength
σ_o	strength of a comparable wrought material
σ_{res}	residual stress
σ_{UTS}	ultimate tensile strength
σ_Y	yield stress
t	time
V_S	fractional density
w	initial-stage sintering constant
W	compact tension specimen width
X	radius of the circle of contact of the particles
Z	initial-stage sintering constant

themselves mechanically within the valleys of the substrate's surface.

There are several advantages associated with the cold-spray technique, most of them resulting from the solid-state nature of the process [10–12]. The low processing temperature results in no bulk particle melting, as well as no deleterious tensile stresses that would otherwise occur in thermal sprayed coatings due to shrinkage during cooling. Furthermore, low temperatures combined with the use of protective gases to carry the feedstock minimize particle oxidation, meaning that oxygen-sensitive materials (e.g. titanium) can be easily deposited. Unlike thermal processes, cold-spray coatings do not exhibit elemental segregation, and there are no changes to the chemical composition or microstructure of the workpiece due to the low levels of heat delivered during the process [13–15]. The significantly high impact velocities of the solid particulates are very effective at peening the underlying material and producing deposits that are typically in a state of compressive stress [16,17]. These compressive residual stresses, combined with the fine microstructure of the deposited cold-spray material, can improve the fatigue life of conventionally manufactured materials. Several studies have proven the advantageous role of the cold-spray coatings in fatigue [18–20]. Specifically, Sansoucy et al. observed that Al-13Co-26Ce cold-spray coatings improved the fatigue life of a 2024-T3 alloy by an order of magnitude (an increase from $\sim 10^6$ to $\sim 10^7$ cycles) at a stress amplitude of 200 MPa [18]. This improvement in the fatigue limit was attributed to the compressive residual stresses introduced in the coatings, and the high adhesion strength of the coatings to the substrate. The results from the work of Ghelichi et al. indicate that the fatigue life of 5052 aluminum alloy cold-spray coated with 7075 alloy was improved up to 30% [20]. Similar conclusions have been reached

in several other publications [21–23].

The limited published data, as well as the lack of understanding of the mechanisms of fatigue crack propagation in cold-spray alloys, are the reasons for conducting this fundamental study. In particular, and for the first time, the long fatigue crack growth behavior of bulk deposited cold-spray 6061 alloy is systematically investigated. The distinction between "long" and "small" fatigue crack growth is very important, especially in the near-threshold regime [24]. Small fatigue cracks can be classified as mechanically-small (comparable in size to local plasticity), microstructurally-small (comparable in size to relevant microstructural characteristic dimensions), and physically-small (cracks not affected by closure, typically less than 1–2 mm in length) [25,26]. This study focuses on long fatigue crack growth behavior, when closure effects need to be taken into account in the near-threshold crack growth regime, Region I [27]. Crack closure can significantly affect the near-threshold applied stress intensity, particularly at lower stress ratios [28,29]. In this study, the Adjusted Compliance Ratio (ACR) was used to calculate the effective closure-corrected stress intensity values (ΔK_{eff}). The ACR method [30] is a crack closure evaluation technique that accounts for the contribution to fatigue crack growth of cyclic crack-tip strain below the opening load, and has been shown to produce accurate, reliable closure-free results [31]. In addition, fatigue crack growth in Regions II and III were also investigated. Fatigue crack growth microstructural mechanisms in cold-spray 6061 have been established for different processing conditions, and design maps and crack growth predictive models have been developed.

2. Methodology

2.1. Materials, processing, and metallographic specimen preparation and microscopy

The powder used by the Army Research Laboratory (ARL) for the preparation of the cold-spray (CS) 6061 depositions was provided by Valimet. The chemical composition of the powder is given in Table 1, compared with a rolled 6061, and the powder particle size and distribution ($25 \mu\text{m} \pm 15 \mu\text{m}$) are shown in Fig. 2. A single batch of powder was used to produce a block of CS 6061 material (size $230 \text{ mm} \times 150 \text{ mm} \times 19 \text{ mm}$) deposited onto a rolled 6061-T6 substrate; all subsequently discussed test specimens were machined from this deposition at least 2.5 mm from the surfaces of the block to avoid sampling material that may not have been fully compacted during the

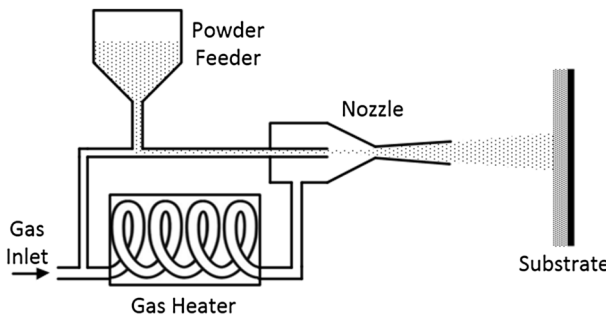


Fig. 1. Schematic of the cold-spray deposition process, adapted from Ref. [4].

Table 1

Chemical composition (in wt%) of cold-spray and rolled 6061 aluminum alloys.

Alloy	Mg	Si	Fe	Cu	Mn	Cr	Ti	Others	Al
Cold-spray 6061	1.01	0.61	0.30	0.25	0.04	0.09	0.02	0.08	Bal.
Rolled 6061	0.90	0.64	0.38	0.26	0.03	0.21	0.02	0.05	Bal.

deposition process.

The cold-spray process deposition parameters are listed in **Table 2**. The deposition process was found to produce no change in the powder's chemical composition or microstructure, as can be seen from the X-ray diffraction patterns presented in **Fig. 3**.

The CS 6061 depositions were evaluated in three conditions: as-sprayed, annealed, and T6. Annealing was performed at 344 °C for 8 h. The T6 heat treatment consisted of solutionizing at 540 °C for 1 h; boiling water quench; and artificial aging at 175 °C for 8 h.

Metallographic specimens were prepared according to ASTM E3-11 and the Buehler SumMet materials preparation guide [32]. Specimens were sectioned using an abrasive cutting wheel. The cut sections were then mounted in Bakelite before grinding and polishing was conducted using an autopolisher. The specimens were etched by immersing in Keller's reagent (95% water, 2.5% HNO₃, 1.5% HCl, 1.0% HF) for 10 s. Optical microscopy was performed using a Nikon MA 200 Eclipse light optical microscope. Representative micrographs were taken, and image analysis was conducted with Nikon's Elements-D software. To establish the fatigue crack propagation mechanisms, fracture surfaces were examined using a JEOL-7000F scanning electron microscope (SEM), and subsequently the specimens were sectioned, mounted, and polished for optical examination of the crack path side profile along the median section.

The microstructures of the as-sprayed, annealed, and T6 CS 6061 depositions were examined in all three dimensions and are shown in **Fig. 4(a)–(c)**. The prior powder particle boundaries are clearly visible, and reveal a slight anisotropy due to the particles being deformed upon impact. The cold-sprayed particle sizes, shown in **Fig. 4(d)–(f)**, were measured using the mean linear intercept method according to the ASTM-112-12 standard [33]. It was observed that both heat treatments increase the mean grain size of the material from ~27 µm in the as-sprayed condition, to ~32 µm and ~36 µm in the annealed and T6 conditions, respectively. The grain size within the powder particles is very fine (< 5 µm); the grains are generally equiaxed except for areas at the edges of the powder particles, where they are slightly deformed due to impact during the cold-spray process. The microstructures of the as-sprayed, annealed, and T6 CS 6061 material are shown in **Fig. 5(a)–(c)**. The microstructure of the as-sprayed CS 6061 material, shown in **Fig. 5(a)**, consists primarily of the α-Al matrix, the Mg₂Si precipitate

Table 2

Substrate and nozzle characteristics and deposition parameters.

Substrate	
Material	6061 aluminum
Substrate Grit Blasting	60 Grit at 414 kPa
Substrate cleaning	Alcohol and air
Nozzle	
Throat diameter	0.0026 m
Weight	0.0647 g
Deposition parameters	
Gas type	Helium
Gas pressure and flow	2000 kPa and 3.0 m ³ /h
Heater set points	Gun at 400 °C and pre-heater at 350 °C
Powder feed actual	1.3 rpm and 13 m ³ /h
Spray distance	0.028 m
Spray gun velocity	1 m/s

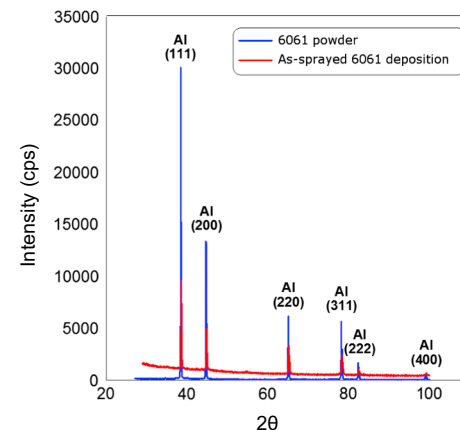


Fig. 3. XRD patterns for the original 6061 powder and as-sprayed 6061 deposition.

phase within the matrix (darker particles), and a mixture of equiaxed and needle-shaped iron-containing Al_xFe_ySi_z phases (lighter particles), primarily located along grain and/or powder-particle boundaries. The precise stoichiometry of these phases is dependent on the alloy composition, and is not established in this study. In the annealed CS 6061 material, shown in **Fig. 5(b)**, the Mg₂Si phase remains unaltered, while some of the acicular Al_xFe_ySi_z phase has become more equiaxed, consistent with findings in the literature [34]. The CS 6061-T6 material, shown in **Fig. 5(c)**, again contains Mg₂Si precipitates, and there is still a significant amount of equiaxed Al_xFe_ySi_z phase present; no evidence of the acicular Al_xFe_ySi_z phase was found. The homogenization of the

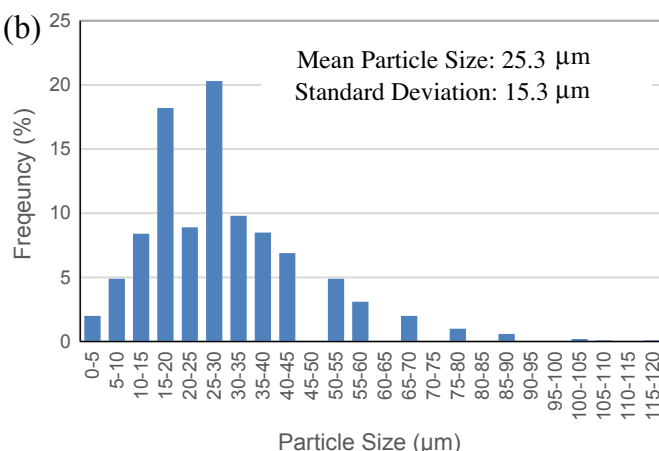
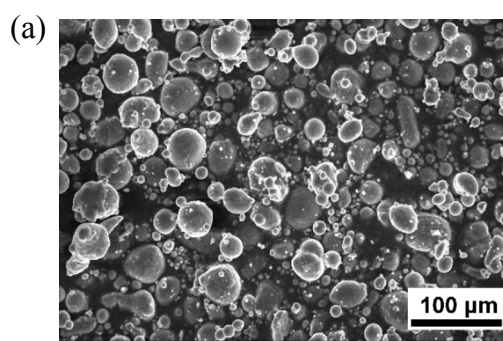


Fig. 2. (a) 6061 powder observed under SEM and (b) 6061 powder particle size distribution.

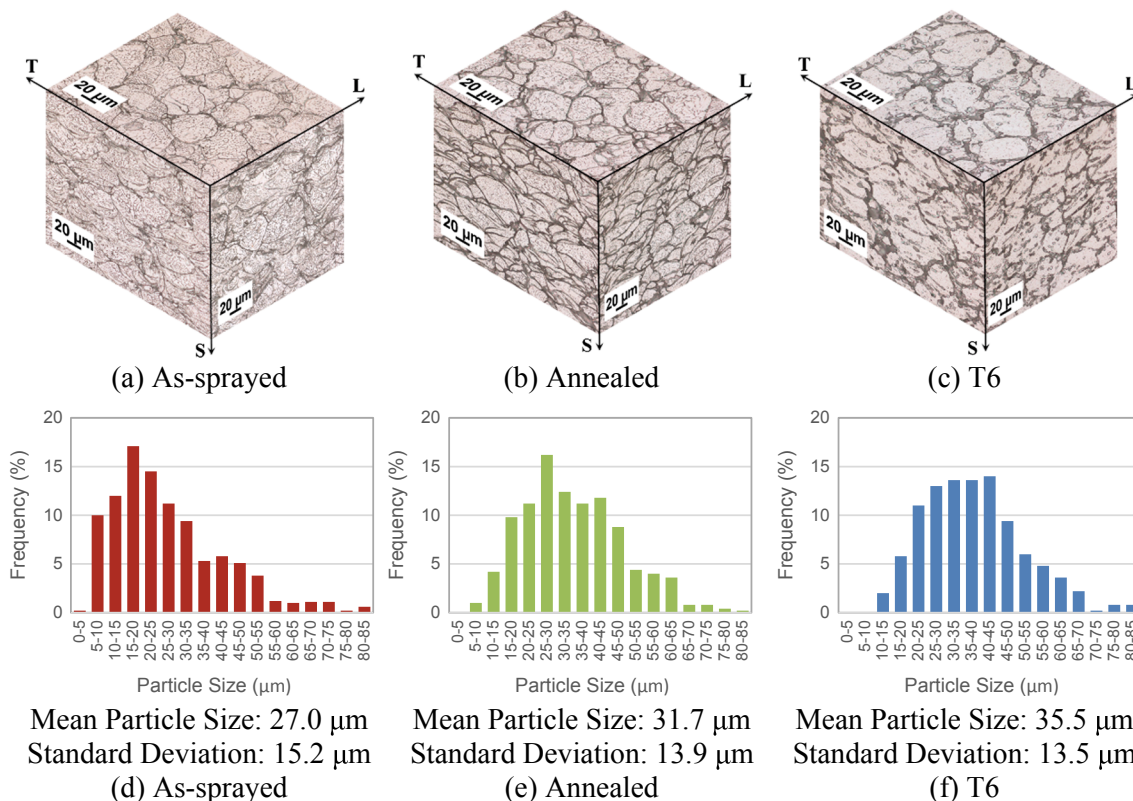


Fig. 4. (a)–(c) Deposition structures, and (d)–(f) particle size distributions, of as-sprayed, annealed, and T6 CS 6061 material.

material has promoted the formation of very small $\text{Al}_{12}(\text{FeCrMn})_3\text{Si}$ dispersoids (50 nm–200 nm), sometimes referred to as the α phase [35,36]. The annealed material may also contain small amounts of very fine dispersoids, although these typically form at temperatures above 375 °C (annealing was performed at 344 °C). The phases found in the three conditions of the cold-spray material are in agreement with simulations conducted in JMat Pro and ThermoCalc, and observations of similar cold-spray alloys by Belsito et al. [37].

A 6061 rolled material (chemical composition given in Table 1) was used in T6 temper as a baseline for comparison purposes. The grain structure consists of recrystallized “pancake” grains, as shown in Fig. 6(a). The microstructure, shown in Fig. 6(b), consists of the α -Al Matrix, Mg_2Si precipitates, $\text{Al}_x\text{Fe}_y\text{Si}_z$ phase along the grain boundaries, which has become fragmented due to the rolling process (from the original needle-like casting phase), and small $\text{Al}_{12}(\text{FeCrMn})_3\text{Si}$ dispersoids.

2.2. Microhardness, tensile, and fatigue crack growth testing

Microhardness measurements were made using a TUKON 1202

tester using a load of 100 gf applied for 10 s. The Vickers microhardness values reported in this study are each average values of 15 individual measurements conducted in accordance with ASTM E384 [38].

The specimens used for tensile testing, shown in Fig. 7(a), were machined with a gauge length of 25 mm and a gauge cross section of 6 × 6 mm. The overall specimen length was 100 mm in order to provide an adequate grip area for testing. Tensile tests were conducted according to ASTM E8/E8M-16a [39] at room temperature in laboratory air, tensile force was applied along the longitudinal (L) direction using a constant strain rate of 0.015 s⁻¹. The strain was measured by an extensometer.

Fatigue crack growth experiments were conducted using compact tension, C(T), specimens, shown in Fig. 7(b). The specimens, with constant thickness, B , of 10.2 mm, and width, W , which varied from 33.0 to 50.8 mm due to original part's size constraints, were machined according to ASTM E647-15, and in compliance with the elastic requirement for all applied loads [40]. The initial notch length (measured from the center of the pinholes) varied between 8.25 and 12.70 mm depending on the width of the specimen. The notch was introduced using wire-cut electrical discharge machining (EDM), and its thickness

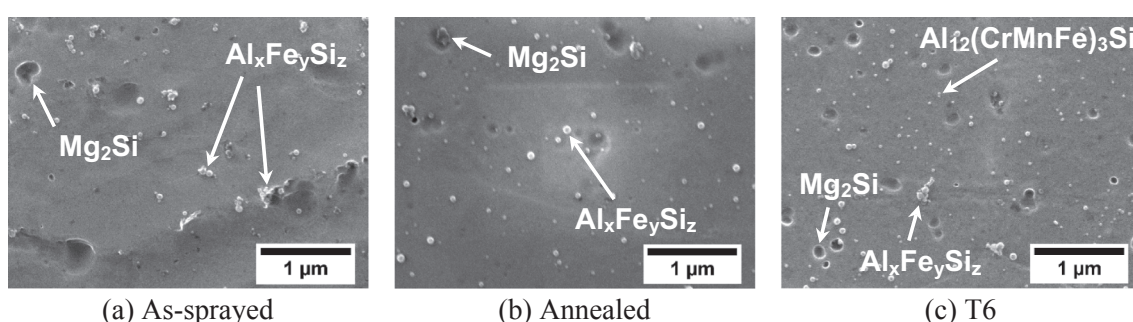


Fig. 5. Secondary electron SEM images of: (a) as-sprayed, (b) annealed, and (c) T6 CS 6061 material.

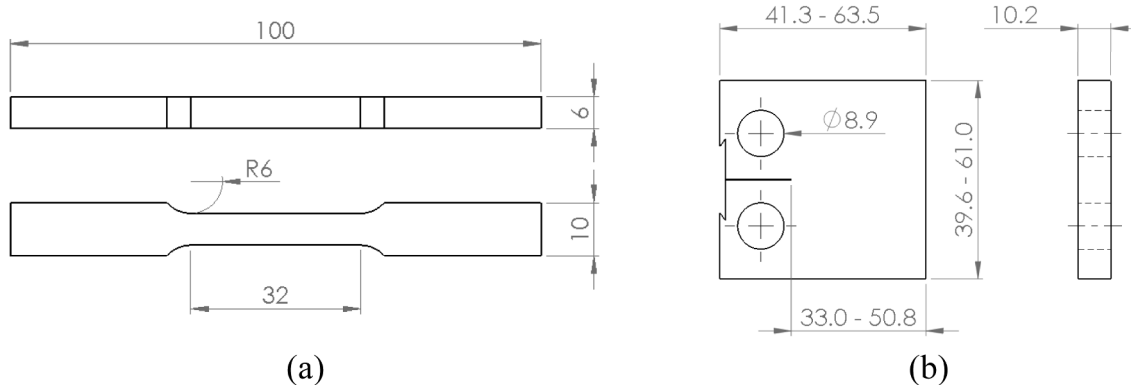
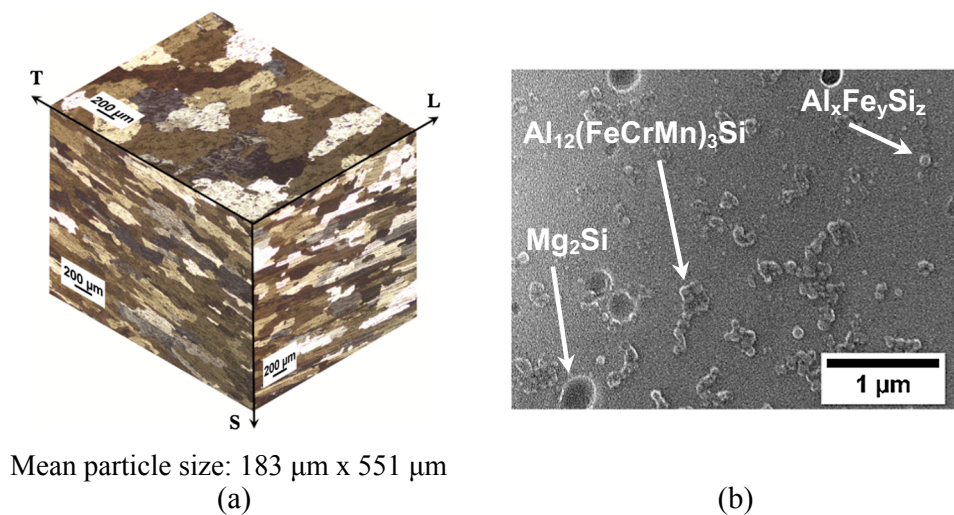


Fig. 7. Schematic drawings of: (a) tensile, and (b) C(T) specimens. All units are in mm; drawings are not to scale.

was 0.254 mm. Fatigue crack growth tests were conducted according to ASTM E647-15 [40], at constant stress ratios ($R = 0.1, 0.5$, and 0.7). The decreasing K method, with a K gradient of -5.5 (MPa/m)/m and frequency of 20 Hz, was used to establish the near-threshold and low Region II fatigue crack growth response. The increasing K method, with a K gradient of $+5.5$ (MPa/m)/m and frequency of 20 Hz, was used to acquire middle and upper Region II and Region III data. Above a crack growth rate of 2.5×10^{-4} mm/cycle, the test was conducted using a constant ΔK and a reduced frequency of 5 Hz in order to capture sufficient data points towards the end of the test. The cracks were grown in the transverse (T) direction, in the ST plane.

Residual stress measurements in the C(T) specimens were taken statically, using the notch clamping method [41], and dynamically during fatigue crack growth testing, at constant ΔK levels (e.g. ~ 8 MPa/m for the annealed CS 6061, and ~ 10 MPa/m for the rolled 6061-T6) [42].

3. Results and discussion

3.1. Microhardness and tensile properties of as-sprayed and heat treated 6061 alloys

The microhardness and static mechanical properties of all studied alloys are presented in Table 3. The microhardness values shown are each an average value from five discreet measurements, each tensile result ($\sigma_{Y(0.2\%)}$, σ_{UTS} , $\epsilon\%_L$, and E) are each an average of three different tensile tests. The results from the tests were consistent, with very little scatter in the data. The fine grain size of the as-sprayed CS 6061 material results in high microhardness and strength, comparable to the

rolled 6061-T6 alloy. However, the Young's moduli of the CS 6061 materials is observed to be lower than the rolled 6061-T6 (most likely due to porosity), and the elongation at failure of the as-sprayed CS 6061 material is significantly lower. The ductility of the CS 6061 is greatly improved by the annealing process, at the expense of the strength. The CS 6061-T6 material has lower microhardness, σ_Y , and σ_{UTS} compared to the as-sprayed condition, and its ductility is similar to that of the as-sprayed condition, and much lower than the annealed value.

3.2. Residual stress evaluations

Prior to the fatigue crack growth testing, the notch clamping/opening at the front face of the C(T) specimens was measured. This information was indicative of whether or not there were any residual stresses in the C(T) specimens, and the type of the stress state, compressive or tensile. From the results in Table 4, it can be concluded that

Table 3

Microhardness, yield strength (σ_Y), ultimate tensile strength (σ_{UTS}), total elongation at failure ($\epsilon\%$), and elastic modulus (E), for all studied alloys; all tests were performed in tension parallel to the longitudinal direction, L, in Fig. 4.

Alloy	Microhardness [HV ₁₀₀]	$\sigma_{Y(0.2\%)}$ (MPa)	σ_{UTS} (MPa)	Elongation ($\epsilon\%$)	E (GPa)
Cold-spray 6061 – As-sprayed	105.0	262.0	286.8	2.0	67.5
Cold-spray 6061 – Annealed	65.7	147.5	195.1	13.0	64.1
Cold-spray 6061 – T6	120.0	203.4	216.5	1.8	65.1
Rolled 6061-T6	107.0	291.6	317.1	17.0	70.3

Table 4

Notch clamping/opening measurements at the front face of the C(T) specimens as averages of five measurements per specimen.

Alloy	Notch clamping/opening [μm]	Stress state
Cold-spray 6061 – As-sprayed	+3.30	Tensile
Cold-spray 6061 – Annealed	+0.25	Tensile
Cold-spray 6061 – T6	-5.33	Compressive
Rolled 6061-T6	-14.98	Compressive

the level of residual stresses in the C(T) specimens was low, consistent with the fact that the specimens were machined from cold-spray deposited blocks.

Although the notch clamping/opening values indicate low average residual stresses in the coupons, the residual stress magnitude at every location of the bulk material is unknown. In order to confirm that the residual stresses were negligible in the bulk material, and to ensure that crack shielding effects in the threshold region, discussed in Section 3.3, were solely due to microstructure, the crack compliance technique [42] was used to obtain the contribution of residual stress to the stress intensity factor, K_{res} , during constant ΔK tests performed on C(T) specimens. The residual stress calculations were performed using the method proposed elsewhere [42]. The results of the residual stress calculations are presented in Fig. 8 for the annealed CS 6061 and rolled 6061-T6 materials. The variations of K_{res} , crack growth rate (da/dN), and residual stress (σ_{res}) with respect to crack length (a) are shown for both 6061 conditions/specimens.

In Fig. 8(a) and (d), the K_{res} values fluctuate around zero, which indicates that the levels of bulk (process-induced) residual stresses are low. The constant crack growth rates during these tests, Fig. 8(b) and (e), are further evidence of low bulk residual stresses in

the specimens. Finally, the residual stress profiles inferred from the K_{res} values, Fig. 8(c) and (f), show uniform and minimal bulk residual stresses in the test specimens. Thus, the fatigue crack growth data presented in the next section are not biased by extrinsic effects, and any shielding effect in the near-threshold regime and low Region II of crack growth is due to the materials' characteristic microstructures.

3.3. Fatigue crack growth data and mechanisms, and microstructure-loading-damage design maps

Fig. 9 and Table 5 summarize the fatigue crack growth results of this study. As discussed in Section 1, for long crack growth the effects of closure need to be taken into account in the near-threshold crack growth regime. The results displayed in Fig. 9 and Table 5 show the applied and effective (ACR corrected [30]) stress intensity ranges (ΔK_{app} and ΔK_{eff} , respectively).

Fatigue crack growth data at $R = 0.1$ for both cold-spray and rolled 6061 material are presented in Fig. 9(a) and (b). In the near-threshold regime, the rolled 6061-T6 material exhibits the highest threshold for crack propagation, followed by the CS 6061-T6, and then the as-sprayed and annealed CS 6061 material. The coarse-grained rolled 6061-T6 material has higher resistance to fatigue crack growth compared to the CS 6061 material, over the entire range of ΔK values. This is in agreement with the trends observed by Pao et al. [43] regarding the fatigue crack growth response of ingot- versus powder-metallurgy Al-Mg alloys. The as-sprayed CS 6061 material has a higher threshold for crack propagation than the annealed CS 6061 material mainly due to higher levels of closure in the as-sprayed material. In the closure corrected data, as shown in Fig. 9(b), the as-sprayed and annealed CS 6061 threshold values are roughly the same. It is important to note that in upper Region II, the annealed CS 6061 material shows higher

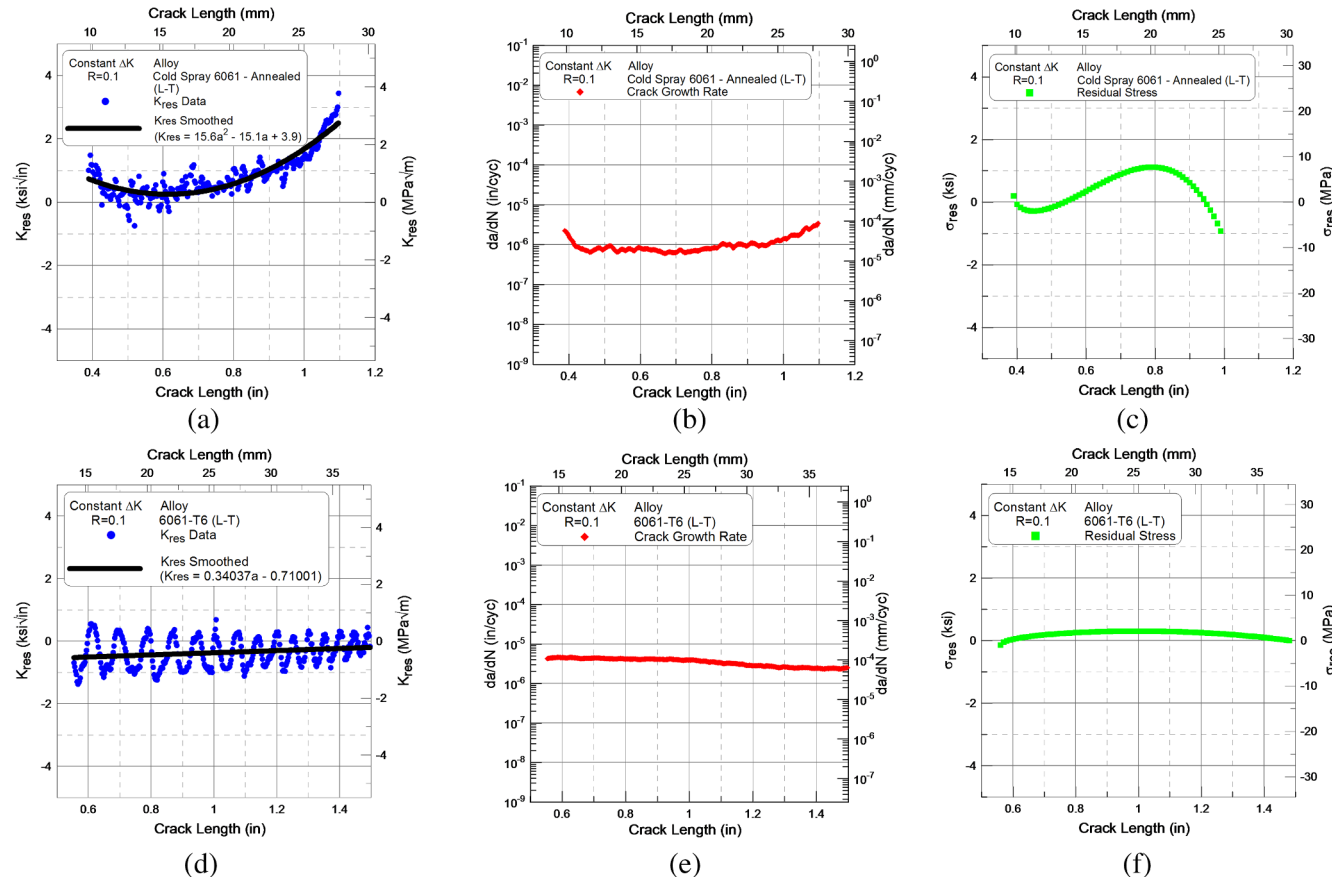


Fig. 8. K_{res} versus a , da/dN versus a , and σ_{res} versus a for (a)–(c) annealed CS 6061, and (d)–(e) rolled 6061-T6 C(T) specimens, tested under constant ΔK conditions in Region II of crack growth.

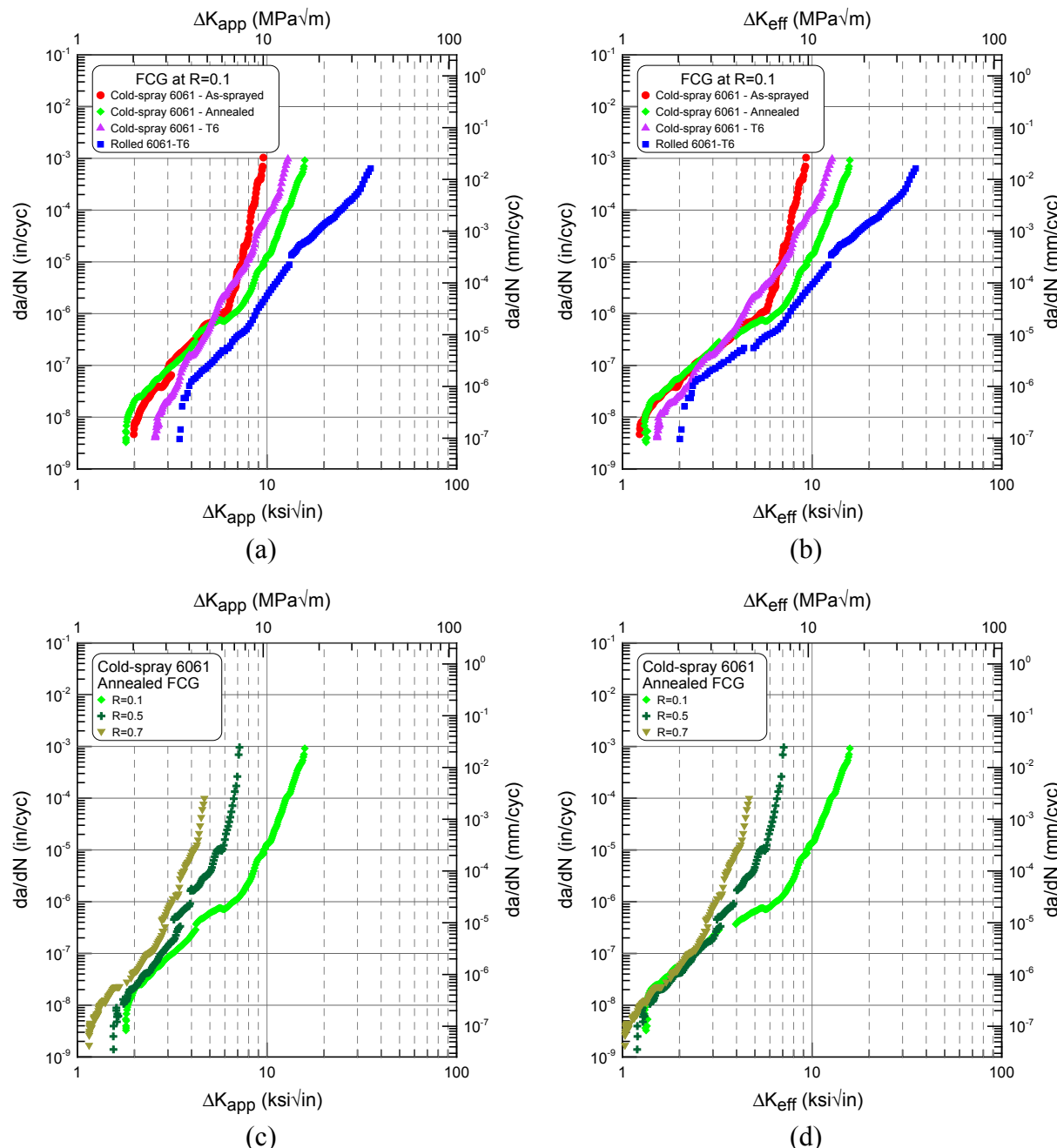


Fig. 9. (a) Applied and (b) ACR-corrected fatigue crack growth data for all CS 6061 material and rolled 6061-T6 at $R = 0.1$; (c) applied and (d) ACR-corrected fatigue crack growth data for annealed CS 6061 material at various stress ratios, $R = 0.1, 0.5$, and 0.7 .

resistance to fatigue crack growth than the other CS 6061 material, especially compared to the as-sprayed CS 6061 material. The enhanced resistance to fatigue crack growth and higher fracture toughness are attributed to the more ductile nature of the annealed CS 6061 material (13% elongation at failure) compared to the as-sprayed and T6 CS 6061 material (both have ~2% elongation at failure), which allows for greater amounts of crack extension before failure. Both the as-sprayed and annealed CS 6061 material, exhibit a transition in the gradient of the fatigue crack growth curve at $\Delta K \sim 6$ MPa \sqrt{m} due to changes in the crack propagation mechanisms associated with the crack tip plastic zone radius, r_p , reaching a critical size. The different crack propagation mechanisms will be assessed further later in this section. This transition is not present in the CS 6061-T6 and rolled 6061-T6 material. In Fig. 9(c) and (d), the effect of stress ratio, R , on the fatigue crack growth response of the annealed CS 6061 material is shown. With increasing R ,

the fatigue crack growth resistance decreases, and the fatigue crack growth curves shift towards lower ΔK values due to gradually higher mean stress levels. In addition, the gradient transition from Region II to Region III becomes less pronounced at higher stress ratios. The applied and ACR-corrected threshold values (ΔK_{th-app} and ΔK_{th-eff}), as well as ΔK_{max} values for all tested conditions are presented in Table 5. The Paris Law constants C and m for Region II of crack growth are also reported.

Complete fracture surface profiles and representative optical side-view, and SEM top-view fractographs from different regions of the fracture surface for all materials and conditions are shown in Figs. 10–15. Overall, the fracture surface profiles of all CS 6061 materials exhibit the same trend. At low ΔK values, in the near-threshold regime and low Region II, crack propagation is transparticular (through the prior-powder particles). With increasing crack tip driving force, at higher ΔK values, a mixed mode of crack propagation is observed, until

Table 5

Summary of the applied and effective ΔK_{th} , ΔK_{max} values, and Paris Law constants (C and m) for all test conditions.

Material	R	ΔK_{th-app} [MPa \sqrt{m}]	ΔK_{th-eff} [MPa \sqrt{m}]	ΔK_{max} [MPa \sqrt{m}]	C	m
Cold-spray 6061	0.1	2.2	1.3	10.2	6.2E−9	3.1
– As-sprayed						
Cold-spray 6061	0.1	2.0	1.4	17.4	8.5E−9	2.8
– Annealed						
Cold-spray 6061	0.5	1.7	1.3	7.8	3.4E−9	3.7
– Annealed						
Cold-spray 6061	0.7	1.3	1.1	5.1	3.6E−9	4.0
– Annealed						
Cold-spray 6061	0.1	2.8	1.6	14.1	1.0E−9	4.7
– T6						
Rolled 6061-T6	0.1	3.8	2.2	38.7	7.3E−9	2.2

the mechanisms change to a completely interparticular (around particles, through particle boundaries) mode in upper Region II – low Region III, where the crack has developed an extensive damage zone ahead of the crack tip to follow favorable particle boundaries, and also iron-containing phases located there. From the fracture surface profile of the rolled 6061-T6 alloy, it is clear that the crack path is very smooth and a transgranular mode of crack advance is observed for the majority of the test, with the exception of few favorably oriented grains for intergranular propagation at the later stages of crack growth, where the static plastic zone radius is larger than the average grain size of the alloy.

In the CS 6061 materials, the fracture surface in the near-threshold regime is smooth, consistent with the transparticular mode of crack propagation, with occasional inflection points at particle boundaries, due to the small powder particle size ($\sim 30 \mu\text{m}$), and the very fine grain structure within them ($< 5 \mu\text{m}$). This fine microstructure of the CS 6061 material results in limited crack shielding and closure, and lower fatigue crack growth thresholds compared to the rolled 6061 material. It is worth noting that after correcting for closure, the CS 6061-T6 material still shows a slightly higher threshold than the as-sprayed and annealed conditions (1.6 MPa \sqrt{m} compared to 1.3 and 1.4 MPa \sqrt{m} , respectively). This implies that differences in the intrinsic microstructural properties, such as the intrinsic resistance of the α -Al matrix, are also

affecting the near-threshold behavior. This is related to the differences in the state of the precipitates and/or dispersoids between the T6 and as-sprayed and annealed conditions.

In Region II, through-particle growth and boundary dimples are evident on the fracture surfaces indicating a mixed mode of crack advance. In the case of the as-sprayed and T6 condition, a relatively brittle mode of crack propagation is observed in Region III, along with some elements of ductile failure at the particle boundaries as indicated by the presence of dimples, Figs. 10 and 14 (right). The annealed CS 6061 material, however, exhibits a very ductile behavior in Region III of fatigue crack growth as shown by the ductile dimples on the entire fracture surface in Fig. 11(right). This ductile behavior can be explained by the relatively high elongation of the annealed CS 6061 material (13% elongation at failure versus $\sim 2\%$ in the other cold-spray conditions). At higher stress ratios ($R = 0.5$ and 0.7), the fracture surfaces of the annealed cold-spray materials show a mixed mode of crack growth in Region II, more dominated by ductile dimples than in the $R = 0.1$ case, indicating a larger amount of interparticular crack growth. This is consistent with the fact that for a similar ΔK value the higher stress ratio cases correspond to more advanced stages of crack growth, dominated by interparticular crack growth mechanisms, as shown in Figs. 12 and 13.

In the case of the rolled 6061-T6 alloy, a faceted appearance is observed in the near-threshold regime, due to the crystallographic nature of crack growth. In Region II, crack propagation is transgranular, and cleavage-like features with planes and steps are evident on the fracture surfaces, indicating a low energy type of crack advance. In the steady-state crack growth regime, fatigue striations were present on the fracture surface of the rolled 6061-T6 alloy. The transgranular growth continues, and striations persistently appear in Region III, until the final stages of crack growth.

Based on fractographic observations under optical and scanning electron microscopes, a two-parameter map that relates the loading conditions (and hence the radius of the crack tip plastic zone, r_p) to fatigue crack growth microstructural mechanisms was constructed for the annealed CS 6061 material using different stress ratios, Fig. 16.

The loading-microstructure-damage mechanisms maps are useful tools for a number of reasons. It can assist in predicting the fatigue crack growth microstructural mechanistic response of the material for the loading conditions of interest. A particular combination of ΔK , K_{max} ,

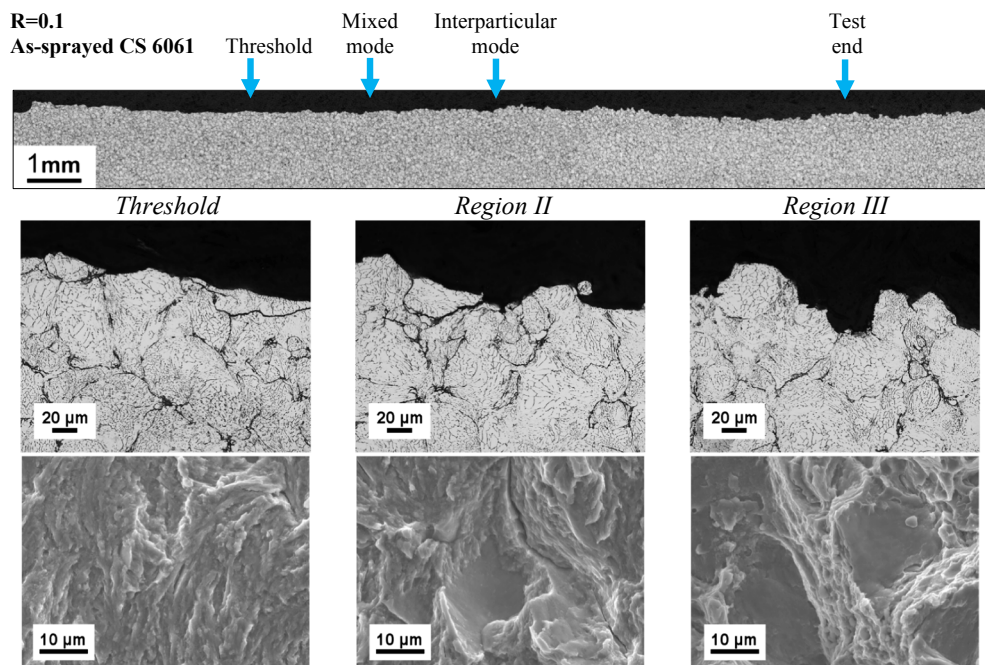


Fig. 10. As-sprayed CS 6061 material crack path profiles and fracture surfaces at various stages of crack propagation at a stress ratio of $R = 0.1$.

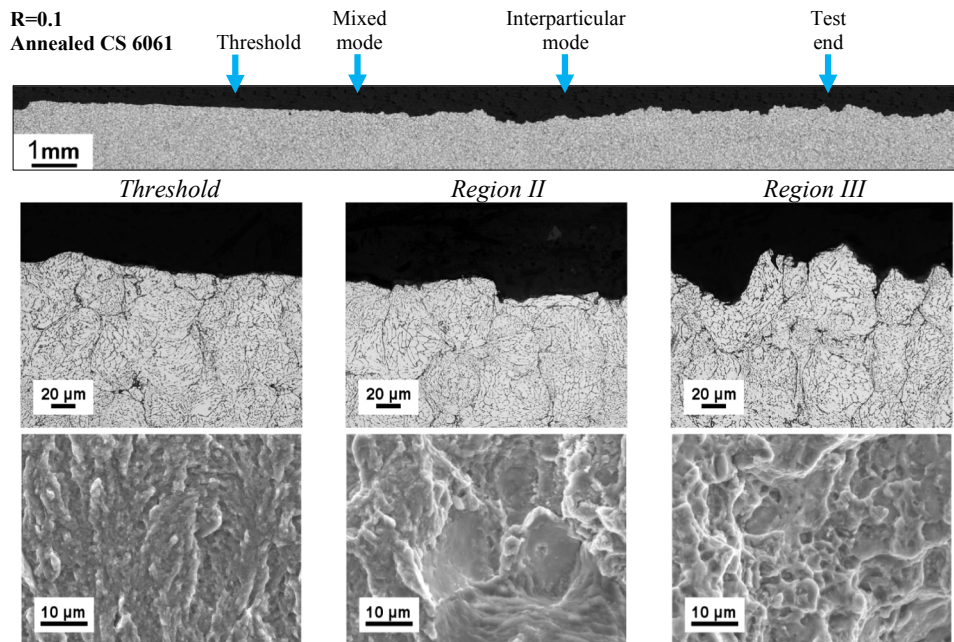


Fig. 11. Annealed CS 6061 material crack path profiles and fracture surfaces at various stages of crack propagation at a stress ratio of $R = 0.1$.

and R , corresponds to a specific point on these two-parameter maps, and depending on the location of that point, a certain mode of crack growth can be anticipated. The map can also be used to help optimize materials and processes for fatigue crack growth resistance based on the type of crack growth, for a given loading scenario. For instance, if for the material and loading conditions of interest the type of crack growth is predicted to be interparticular, designers will need to alter either the loading parameters (if the application allows) or the material's microstructure through processing in order to operate in the safer transparticular crack growth regime. Furthermore, the information collected from such maps can aid in properly selecting the inspection intervals for actual engineering components, thus lowering maintenance cost and time (e.g. inspection intervals could be extended when crack growth is known to be in the transparticular mode, and shortened when cracks approach the less predictable mixed transparticular and interparticular mode).

3.4. Analytical models for predicting fatigue crack growth in cold-spray alloys

A model was developed to describe fatigue crack growth behavior in upper Region II and Region III, as well as fracture toughness of cold-spray alloys, where grain boundaries play a dominant role, and it was further used to quantify the differences observed between the as-sprayed and annealed CS 6061 material. It was observed that at approximately 2×10^{-5} mm/cycle and 6 MPa/m, crack growth becomes predominantly interparticular. Thus, the strength of the bond between the cold-spray particles plays a critical role in the crack's advance in upper Region II and Region III. In addition, the ductility of the CS 6061 material significantly affects the resistance to fracture. Both bond strength and ductility are related to the annealing heat treatment, which changes the interparticle bond strength by the diffusion processes. According to the strength model by Xu et al. [44], the bond strength between particles is dependent on the neck size to particle

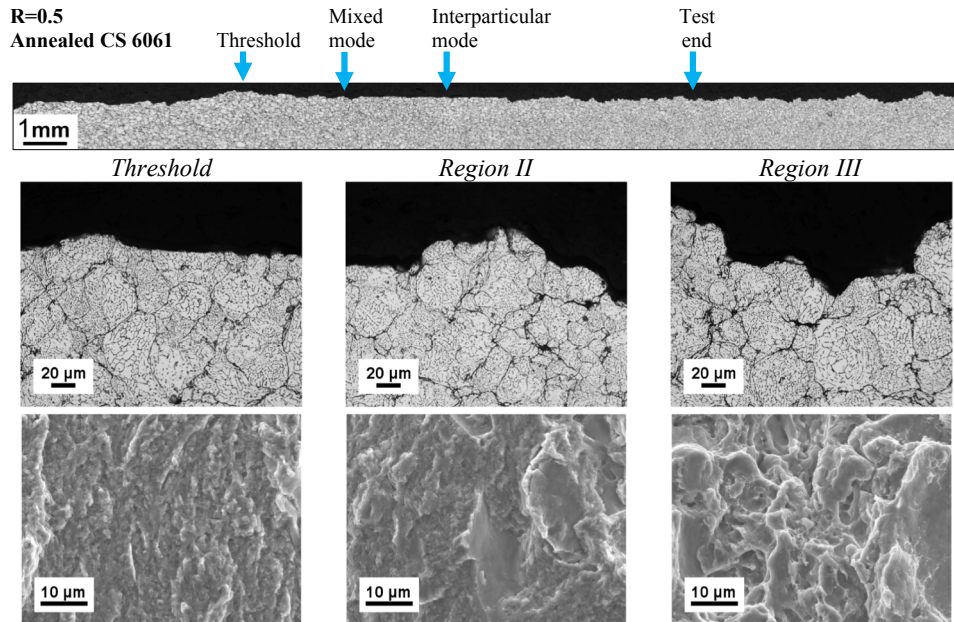


Fig. 12. Annealed CS 6061 material crack path profiles and fracture surfaces at various stages of crack propagation at a stress ratio of $R = 0.5$.

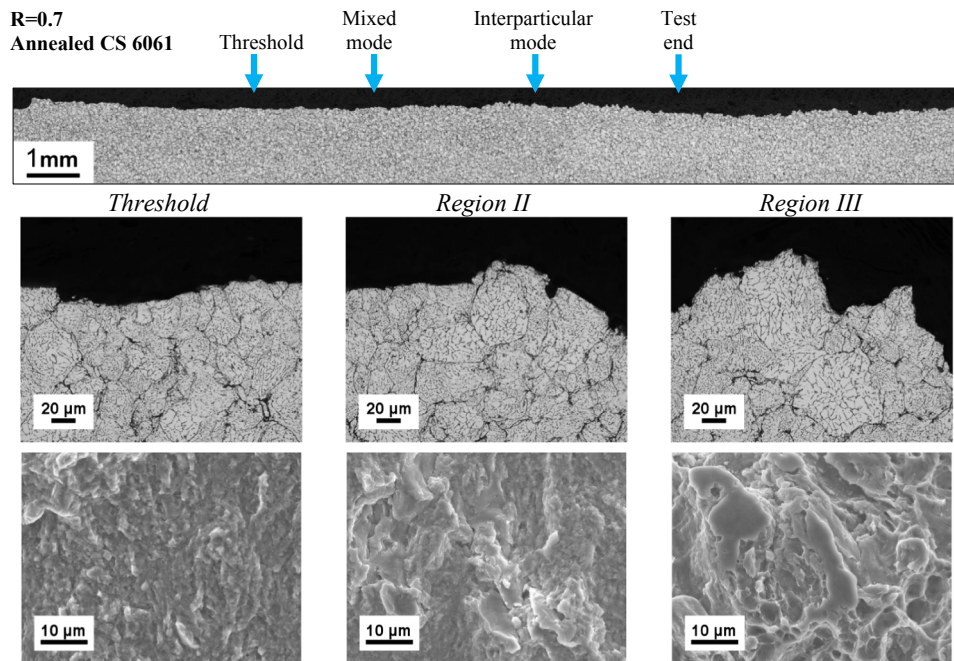


Fig. 13. Annealed CS 6061 material crack path profiles and fracture surfaces at various stages of crack propagation at a stress ratio of $R = 0.7$.

diameter ratio, X/D , and stress concentration factor, F , associated with the interparticle neck, along with the other parameters, as given in the following equation:

$$\sigma_B = f_T \sigma_o V_s \left(\frac{N_c}{F\pi} \right) \left(\frac{X}{D} \right)^2 \quad (1)$$

where f_T is the thermal softening fraction, σ_o is the strength of a comparable wrought material, V_s is the fractional density, N_c is the average particle packing coordination number, X is the bond neck size, and D is the particle diameter. The annealing process causes the neck size to particle diameter ratio to increase, and the interparticle bond to strengthen, as demonstrated schematically in Fig. 17.

The average particle packing coordination number, N_c , is related to

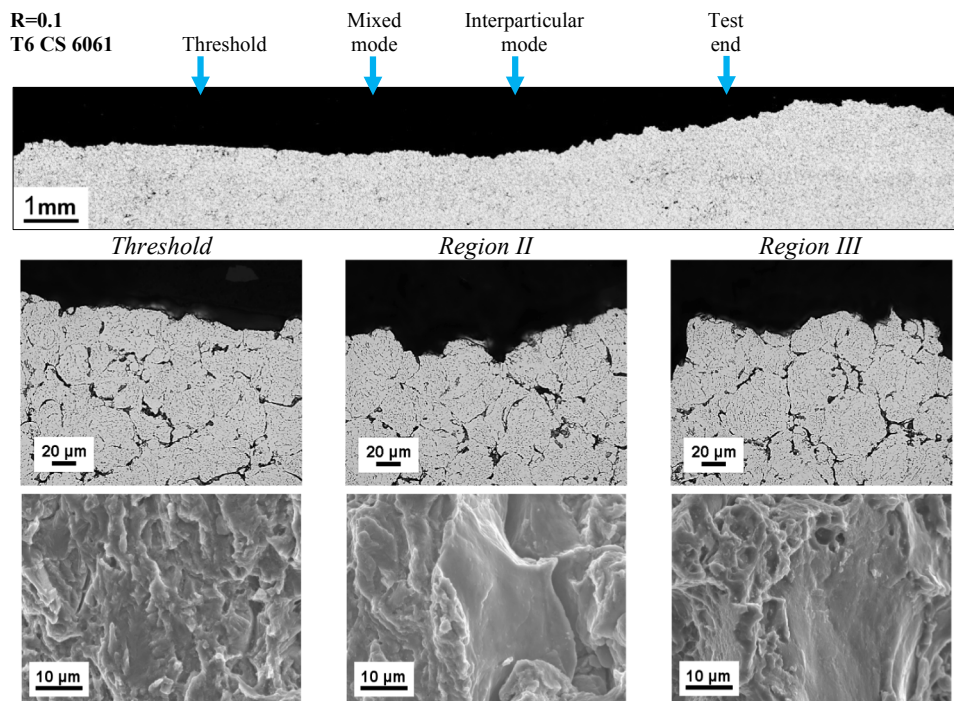


Fig. 14. CS 6061-T6 material crack path profiles and fracture surfaces at various stages of crack propagation at a stress ratio of $R = 0.1$.

the fractional density, V_s , as given in the following equation [44]:

$$N_c = 14 - 10.3(1 - V_s)^{0.38} \quad (2)$$

The stress concentration factor, F , is inversely proportional to the curvature at the base of the neck, which depends on the neck size to particle diameter ratio, as given in the following equation [44]:

$$F = \frac{1}{2} \left(\frac{D}{X} \right)^2 \quad (3)$$

During an isothermal treatment, neck growth can take place, and depending on the time of treatment, the bond strength can vary significantly. The neck size, X , can be predicted by the following equation [45]:

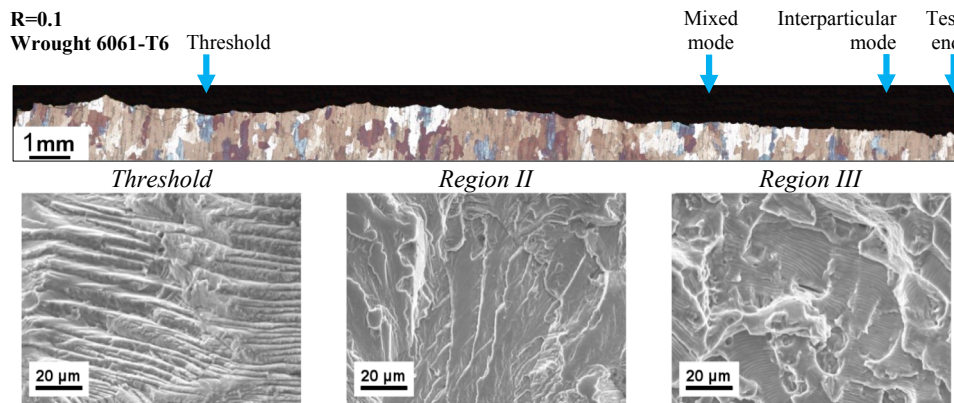


Fig. 15. Rolled 6061-T6 substrate material crack path profile and fracture surfaces at various stages of crack propagation at a stress ratio of $R = 0.1$.

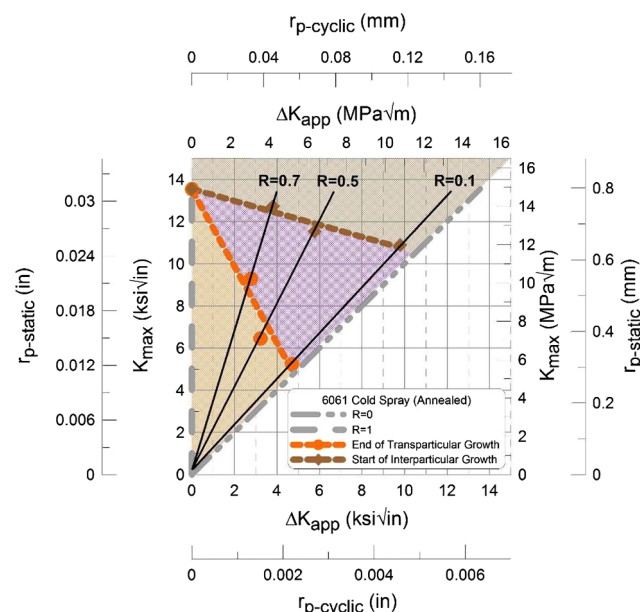


Fig. 16. Two-parameter loading-microstructure-damage mechanisms design map for the annealed CS 6061 material.

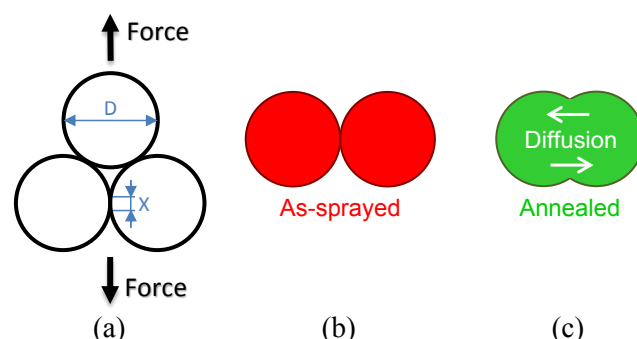


Fig. 17. (a) Schematic of spherical particles showing the bond area for (b) as-sprayed and (c) annealed conditions, with the bond area increasing due to inter-particle diffusion during annealing.

$$\left(\frac{X}{D}\right)^w = \frac{bt}{D^z} \quad (4)$$

where w , b , and Z are initial stage sintering constants based on material, process, and mechanism variables shown in Table 6 [45], and t is the sintering time. These equations allow the prediction of the bond strength for different processing parameters during an isothermal treatment. It is important to note though, that in the case of CS 6061

material, the residual strain in the material after deposition is the driving force for annealing and softening of the material during an isothermal treatment, and this is considered in the model by the thermal softening fraction term, f_T , which can be determined from existing tensile strength data at various temperatures [46]. Fig. 18 shows the variation of the thermal softening fraction with respect to the homologous temperature (temperature expressed as a fraction of the materials melting point) for a wrought 6061-T6 alloy. It is assumed that the CS 6061 material exhibit similar thermal softening behavior.

The diffusion related term is dependent on the dominant mechanism(s) of neck growth. A list of the main mechanisms that contribute to neck growth, as well as the respective expressions for the b term are given in Table 6 [45].

In this study, three main mechanisms were considered: volume, grain boundary, and surface diffusion. The neck size for the annealed CS 6061 material was calculated for a temperature of 344 °C and time of 8 h. From Eqs. (2)–(4), and the thermal softening fraction, Fig. 18, the bond strength of the as-sprayed and annealed CS 6061 material can be calculated.

Given the linear behavior of the da/dN versus ΔK correlation in Region III, shown in Fig. 9(a), a Paris-type law is proposed to predict the linear fatigue crack growth rates observed in upper Region II and Region III, as shown in the following equations:

$$\frac{da}{dN} = C'(\Delta K)^{m'} \quad (5)$$

$$\log\left(\frac{da}{dN}\right) = \log(C') + m'\log(\Delta K) \quad (6)$$

The constants C' and m' are material dependent since the environment, test frequency, and specimen thickness were kept consistent. Specifically, the m' parameter defines the slope of the fatigue crack growth curves, and $\log(C')$ the intercept on the crack growth rate axis when the growth rates are plotted against the cyclic stress intensity factor range on a log-log scale.

The m' parameter can further be expressed as a function of materials' properties and stress ratio, as shown in the following equation:

$$m' = \left(\frac{\sigma_Y}{\sigma_B}\right)^3 \cdot \frac{q}{\sqrt{1 + sR + uR^2 + vR^3}} \quad (7)$$

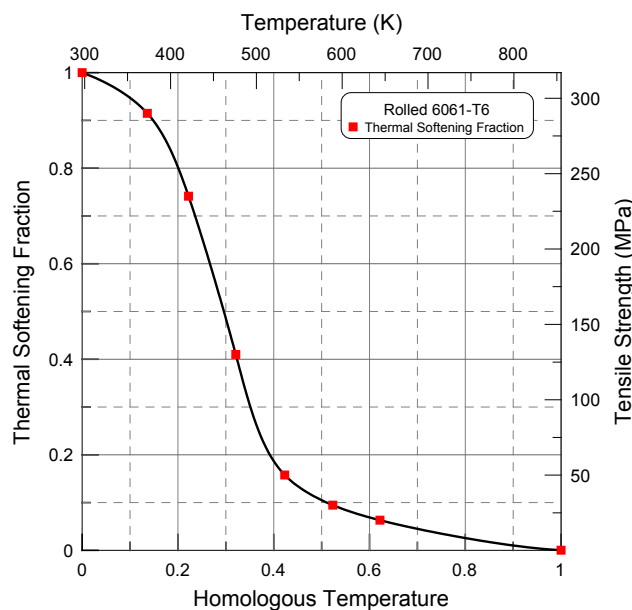
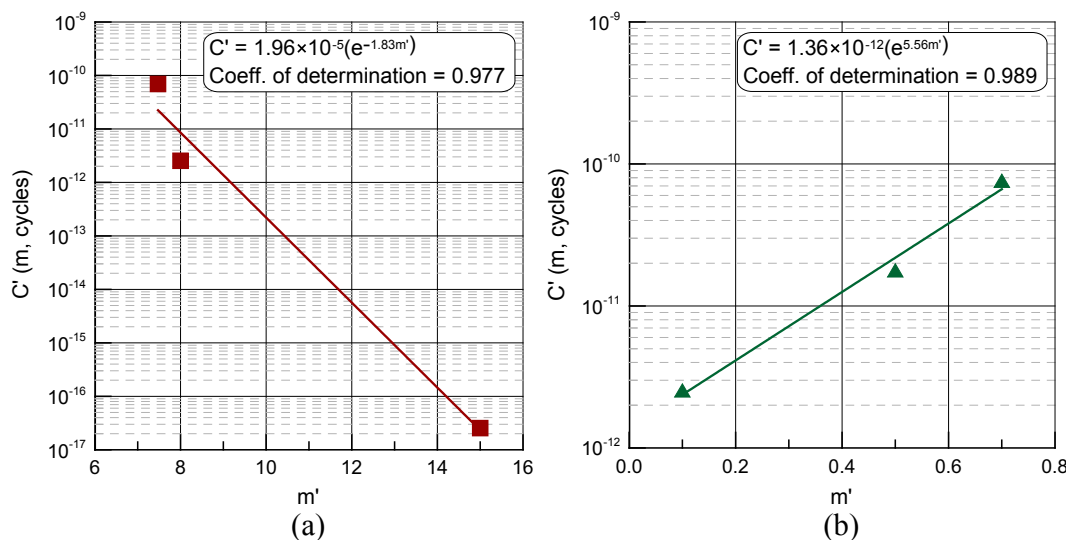
where the exponent 3, q , s , u , and v are fitting parameters to account for stress ratio effects. This formulation was developed on the basis of indirectly incorporating the degree of the alloy's ductility since it controls the behavior in this regime of crack growth. When the ratio of the yield strength to bond strength approaches unity, the material exhibits a brittle type of behavior, and the slope of the fatigue crack growth curve increases. The influence of the stress ratio on the slope of the fatigue crack growth curves was taken into account using an empirical formulation in Eq. (7).

The C' parameter can be then derived through a regression analysis,

Table 6

Main neck growth mechanisms and their analytical expressions [45].

Mechanism	w	z	b	Symbol definition
Viscous flow	2	1	$\frac{3\gamma}{2\eta}$	γ = surface energy η = viscosity
Plastic flow	2	1	$\frac{9\pi b D_v}{kT}$	b = Burgers vector D_v = volume diffusivity k = Boltzmann's constant
Evaporation-condensation	3	2	$\left(\frac{3P\gamma}{\rho^2}\right)\left(\frac{\pi}{2}\right)^{1/2}\left(\frac{M}{kT}\right)^{3/2}$	T = absolute temperature P = vapor pressure ρ = theoretical density M = molecular weight
Volume diffusion	5	3	$\frac{8D_v\gamma\Omega}{kT}$	Ω = atomic volume
Grain boundary diffusion	6	4	$\frac{20\delta D_B\gamma\Omega}{kT}$	δ = grain boundary width D_B = grain boundary diffusivity
Surface diffusion	7	4	$\frac{56D_s\gamma\Omega^{4/3}}{kT}$	D_s = surface diffusivity

**Fig. 18.** Thermal softening fraction versus homologous temperature for rolled 6061-T6 material.**Fig. 19.** (a) Intercept versus slope at $R = 0.1$, and (b) intercept versus stress ratio, R , for the annealed CS 6061 material.

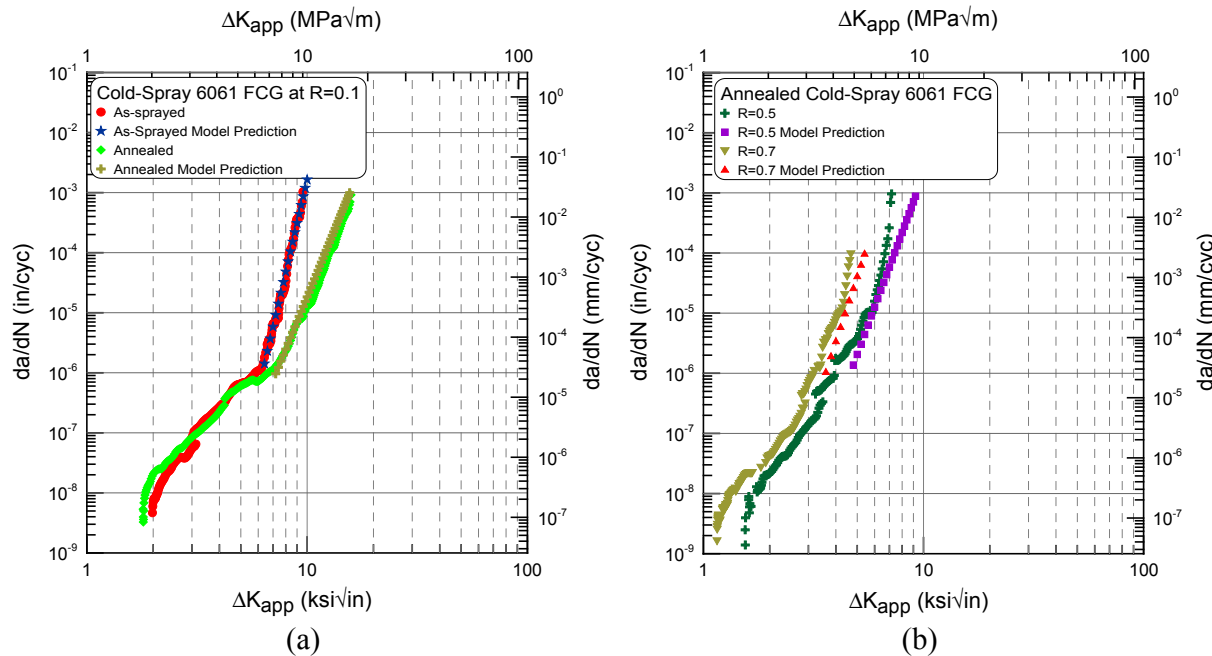


Fig. 20. Experimental and predicted fatigue crack growth data for: (a) as-sprayed and annealed alloys at $R = 0.1$, and (b) annealed alloys at $R = 0.5$ and 0.7 .

undergo post-deposition isothermal treatments. The high ΔK region of the fatigue crack growth curve is particularly important for materials and components designed for low cycle fatigue (LCF) applications and impact resistance.

Combining this model with the use of the loading-microstructure-damage mechanisms map, shown in Fig. 16, will allow the optimization of post-cold-spray heat treatment processes for cold-spray components, coatings, and repairs, where powder particle boundaries can be controlled through post-deposition treatments for enhanced fatigue crack growth resistance and higher fracture toughness.

4. Summary and conclusions

Cold-spray alloys have appealing mechanical properties and have the potential for use in structural applications. They have a fine microstructure made up of consolidated powder particles with fine grains within. The annealing and T6 heat treatments to CS 6061 material caused a slight increase in the initial particle size due to diffusion taking place at particle boundaries.

The as-sprayed CS 6061 material was found to have comparable microhardness and strength to the rolled 6061-T6 material, but the ductility was notably lower. The ductility of CS 6061 material was greatly improved by the annealing heat treatment, and recent enhancements in the deposition process are able to attain higher ductility directly in the as-sprayed condition.

The rolled 6061-T6 material has higher resistance to fatigue crack growth compared to the CS 6061 material over the entire range of ΔK values. The CS 6061-T6 material has a higher ΔK_{th} than the as-sprayed and annealed CS 6061 material due to the stronger matrix of the T6 material inhibiting crack growth at low ΔK . The as-sprayed CS 6061 material was found to have a slightly higher crack growth threshold than the annealed one, related to the higher roughness-induced closure observed in the as-sprayed CS 6061 material. However, the annealing heat treatment was found to significantly improve the fatigue crack growth behavior of CS 6061 material at higher ΔK values, as well as the fracture resistance, due to enhanced ductility and better inter-particle bonding.

Fracture surface examinations indicate a transition in crack growth mechanisms from transparticular to interparticular with increasing ΔK , indicating that particle boundaries have an important effect on the fatigue crack growth response of the cold-spray material, especially at high driving force. Fractographic observations of the fracture surfaces and crack paths were used to develop loading-microstructure-damage mechanisms design maps, which link loading scenarios to the fatigue crack growth mechanistic response at the scale of the cold-spray alloy microstructures, representing valuable tools for material, process, and operating conditions optimization.

For the as-sprayed and annealed CS 6061 material, a linear relationship between da/dN and ΔK was observed on the log-log scale in upper Region II and Region III of crack growth. Thus, a Paris-type model was developed to predict the fatigue crack growth rates of the cold-spray materials at high ΔK , based on processing parameters and materials characteristics. This model, in combination with the loading-microstructure-damage mechanisms maps, can be used to optimize the post-cold-spray isothermal treatments for cold-spray components, coatings, and repairs, where powder particle boundaries can be controlled for enhanced fatigue crack growth resistance and higher fracture toughness, resulting in improved overall component life.

This work provides unique insight on the fatigue crack growth microstructural mechanisms of cold-spray material, as well as tools that can be used for material-process optimization and fatigue crack growth predictions in Regions II and III. A successive study on small fatigue crack growth and mechanisms in Region I, and the stability at the interface between cold-spray coatings and substrates during loading will be presented subsequently.

Acknowledgements

The authors thank the consortium members of the Integrative Materials Design Center at Worcester Polytechnic Institute, and especially the Army Research Laboratory (ARL), for their support of this work. The authors also thank Dr. Nick Parson of Rio Tinto Aluminum for his assistance with the phase identification in the cold-spray and rolled 6061 alloys.

References

- [1] Assadi H, Gartner F, Stoltenhoff T, Kreye H. Bonding mechanisms in cold gas spraying. *Acta Mater* 2003;51:4379–94.
- [2] Grujicic M, Zhao C, DeRosset W, Helfritch D. Adiabatic shear instability based mechanisms for particles/substrate bonding in the cold-gas dynamic-spray process. *Mater Des* 2004;25:681–8.
- [3] Schmidt T, Gartner F, Assadi H, Kreye H. Development of a generalized parameter window for cold spray deposition. *Acta Mater* 2006;54:729–42.
- [4] Champagne V, Helfritch D, Leyman P, Lempicki R, Grendahl S. The effects of gas and metal characteristics on sprayed metal coatings. *Model Simul Mater Sci Eng* 2005;13:1119–28.
- [5] Cavaliere P, Silvello A. Fatigue behaviour of cold sprayed metals and alloys: critical review. *Surf Eng* 2016;32:631–40.
- [6] Champagne V, Helfritch D, Dinavahi S, Leyman P. Theoretical and experimental particle velocity in cold spray. *J Therm Spray Technol* 2010;32. Published online.
- [7] Raletz F, Vardelle M, Ezoo G. Critical particle velocity under cold spray conditions. *Surf Coat Technol* 2006;20:1942–7.
- [8] Grujicic M, Saylor J, Beasley D, Derossset W, Helfritch D. Computational analysis of the interfacial bonding between feed-powder particles and the substrate in the cold-gas dynamic-spray process. *Appl Surf Sci* 2003;219:211–27.
- [9] Hussain T, McCartney DG, Shipway PH, Zhang D. Bonding mechanisms in cold spraying: The contributions of metallurgical and mechanical components. *J Therm Spray Technol* 2009;18(3):364–79.
- [10] Papyrin A. Cold spray technology. *Adv Mater Processes* 2001;159:49–51.
- [11] Champagne V, Helfritch D. The unique abilities of cold spray deposition. *Int Mater Rev* 2016;61:437–55.
- [12] Modern cold spray: materials, process, and applications. Springer International Publishing; 2015.
- [13] Davies JR. Handbook of thermal spray technology; 2004.
- [14] Pawlowski L. The science and engineering of thermal spray coatings, second ed.; 2008.
- [15] Clyne TW, Gill SC. Residual stresses in thermal spray coatings and their effect on interfacial adhesion: A review of recent work. *J Therm Spray Technol* 1996;5:401.
- [16] Champagne V, editor. The cold spray materials deposition process: fundamentals and applications. Cambridge, U.K.: Woodhead Publishing Limited; 2007.
- [17] Cavaliere P, Silvello A. Processing conditions affecting residual stresses and fatigue properties of cold spray deposits. *Int J Adv Manuf Technol* 2015;81:1857–62.
- [18] Sansoucy E, Kim G, Moran A, Jodoin B. Mechanical characteristics of Al-Co-Ce coatings produced by the cold spray process. *J Therm Spray Technol* 2007;16:651–60.
- [19] Kim G, Jodoin B, Sansoucy E. Use of cold spray to deposit coatings which improve fatigue life of a component; 2008.
- [20] Ghelichi R, MacDonald D, Bagherifard S, Jahed H, Guagliano M, Jodoin B. Microstructure and fatigue behavior of cold spray coated Al5052. *Acta Mater* 2012;60:6555–61.
- [21] Ghelichi R, Bagherifard S, MacDonald D, Brochu M, Jahed H, Jodoin B, et al. Fatigue strength of Al alloy cold sprayed with nanocrystalline powders. *Int J Fatigue* 2014;65:51–7.
- [22] Moridi A, Hassani-Gangaraj SM, Vezzù S, Trško L, Guagliano M. Fatigue behavior of cold spray coatings: The effect of conventional and severe shot peening as pre-/post-treatment. *Surf Coat Technol* 2015;283:247–54.
- [23] Sun W, Tan AWY, Khun NW, Marinescu I, Liu E. Effect of substrate surface condition on fatigue behavior of cold sprayed Ti6Al4V coatings. *Surf Coat Technol* 2017;320:452–7.
- [24] Lados DA, Apelian D, Donald JK. Fatigue crack growth mechanisms at the microstructure scale in Al-Si-Mg cast alloys: Mechanisms in the near-threshold regime. *Acta Mater* 2006;54:1475–86.
- [25] Suresh S, Ritchie RO. Propagation of short fatigue cracks. *Int Met Rev* 1984;29:445–75.
- [26] Ritchie RO, Lankford J. Small fatigue cracks: A statement of the problem and potential solutions. *Mater Sci Eng* 1986;84:11–6.
- [27] Lados DA, Apelian D, Paris P, Donald J. Closure mechanisms in Al-Si-Mg cast alloys and long-crack to small-crack corrections. *Int J Fatigue* 2005;27:1463–72.
- [28] Vasudevan AK. A review of crack closure, fatigue crack threshold and related phenomena. *Mater Sci Eng A* 1994;188:1–22.
- [29] Elber W. The significance of fatigue crack closure. *ASTM STP 486 - Damage Tolerance in Aircraft Structures* 1970:230–42.
- [30] Donald K. Introducing the compliance ratio concept for determining effective stress intensity. *Int J Fatigue* 1997;19:191–5.
- [31] Donald K. An evaluation of the adjusted compliance ratio technique for determining the effective stress intensity factor. *Fatigue Fract Mech* 1999;29:674–95.
- [32] Buehler SumMet, The sum of our experience a guide to materials preparation and analysis, second ed.; 2013.
- [33] ASTM, E112-12 standard test methods for determining average grain size; 2012.
- [34] Jeniski Jr RA. Effects of Cr addition on the microstructure and mechanical behaviour of 6061-T6 continuously cast and rolled redraw rod. *Mater Sci Eng A* 1997;237:52–64.
- [35] Du P, Yan XD, Li YL, Shen J. Transformation mechanism of iron-rich phase in 6061 aluminum alloy during homogenization. *Chin J NonFerr Met* 2011;21:981–7.
- [36] Buchanan K, Ribis J, Garnier J, Colas K. Identification of monoclinic O-phase disperoids in a 6061 aluminium alloy. *Philos Mag* 2016;96:121–31.
- [37] Belsito D, McNally B, Bassett L, Champagne V, Sisson R. Proceedings of MS&T, Montreal, Canada; 2013.
- [38] ASTM, E384-11 standard test method for knoop and vickers hardness of materials; 2011.
- [39] ASTM, E8/E8M-16a standard test methods for tension testing of metallic materials; 2016.
- [40] ASTM, E647-15 Standard test method for measurement of FCG rates; 2015.
- [41] Lados DA, Apelian D. The effect of residual stress on the fatigue crack growth behavior of Al-Si-Mg cast alloys - Mechanisms and corrective mathematical models. *Metall Trans A* 2006;37A:133–45.
- [42] Lados DA, Apelian D, Donald JK. Fracture mechanics analysis for residual stress and crack closure corrections. *Int J Fatigue* 2007;29:687–94.
- [43] Pao PS, Jones HN, Cheng SF, Feng CR. Fatigue crack propagation in ultrafine grained Al-Mg alloy. *Int J Fatigue* 2004;27:1164–9.
- [44] Xu X, Lu P, German RM. Densification and strength evolution in solid-state sintering Part II Strength model. *Int J Mater Sci* 2002;37:117–26.
- [45] German RM. Sintering theory and practice. John Wiley & Sons; 1996.
- [46] ASM specialty handbook: aluminum and aluminum alloys; 2002.